Atmospheric
Measurement
Techniques
Discussions

1 # Optimizing a twin-chamber system for direct ozone production rate

2 # measurement

3 Yaru Wang[1#], Yi Chen[2#], Suzhen Chi[1#], Jianshu Wang[1], Chong Zhang[1], Weixiong Zhao[3], Weili Lin[2],
4 Chunxiang Ye[1*]

5 [1]State Key Joint Laboratory for Environmental Simulation and Pollution Control, Center for Environment and Health, and
6 College of Environmental Sciences and Engineering, Peking University, Beijing, 100871, China.
7 [2]Key Laboratory of Ecology and Environment in Minority Areas (Minzu University of China), National Ethnic Affairs
8 Commission, Beijing, 100081, China.
9 [3]Laboratory of Atmospheric Physico-Chemistry, Chinese Academy of Sciences Hefei Institutes of Physical Science Anhui
10 Institute of Optics and Fine Mechanics, Chinese Academy of Sciences, Hefei, 230031, Anhui, China.
11
12 [#]Yaru Wang, Yi Chen and Suzhen Chi contribute equally to this work.

13 [*]*Correspondence to*: Chunxiang Ye (c.ye@pku.edu.cn)

14
15
16
17
18
19
20
21
22
23
24
25
26
27
28
29
30
31
32   A manuscript submitted to *AMT*

33 **Abstract.** High Ozone Production Rate (OPR) leads to O_3 pollution episodes and adverse human health outcomes.
34 Discrepancies between OPR observation (Obs-OPR) and OPR modeling (Mod-OPR) as calculated from observed and modeled
35 peroxy radical and nitrogen oxides reminds of a yet-perfect understanding of O_3 photochemistry. Direct measurement of OPR
36 (Mea-OPR) by a twin-chamber system emerges with the optimization required for suppressing the wall effect. Herein, we
37 minimized the chamber surface area to volume ratio (S/V) to 9.8 m^{-1} and the dark uptake coefficient of O_3 to the order of 10^{-9}.
38 Condition experiments further revealed a photo-enhanced O_3 uptake and recommended an essential correction. We finally
39 characterized a measurement uncertainty of ±27% and a detection limit of 2.8 ppbv h^{-1} (3SD), which suggests that Mea-OPR
40 is sensitive enough to measure OPR in urban or suburban environments. Application of this system in urban Beijing during
41 the Winter Olympic Games recorded a noontime OPR of 7.4 (±3.8, 1SD) ppbv h^{-1}, which indicates fairly active O_3
42 photochemistry despite the pollution control policy implemented. Mea-OPR *versus* $j(O^1D)$ slope of 6.1 × 10^5 ppbv h^{-1} s^{-1}
43 confirmed fairly active O_3 photochemistry, which was assisted by a high abundance of VOCs and NO_x, atypically high Mea-
44 OPR even under high-NO_x conditions, but mediated by relatively weak ultraviolet (UV) radiation.
45

46 **Short summary.** We reported an optimized system (Mea-OPR) for direct measurement of ozone production rate, which
47 showed a precise, sensitive and reliable measurement of OPR for at least urban and suburban atmosphere, and active O_3
48 photochemical production in winter Beijing. Herein, the Mea-OPR system also shows its potential in exploring the fundamental
49 O_3 photochemistry, i.e., surprisingly high ozone production even under high-NO_x conditions.
50

51

52

53

54

55

56

57

58

59

60

61

62

Atmospheric
Measurement
Techniques
Discussions

Open Access

1 Introduction

63

64   Tropospheric ozone (O_3) is a hazardous air pollutant and a key product of photochemical smog (Prinn, 2003; Sillman, 2003).

65   The growing abundance of O_3 due to primarily photochemical production has long been associated with the human health risk

66   (Ho et al., 2007), plant growth issues (Ashmore, 2005), and climate change (Forster et al., 2007). Understanding why the O_3

67   level continues increasing in some regions, despite rigorous emissions control policy (Tarasick et al., 2019), is vital to reverse

68   the O_3 increasing trend.

69   In favorable meteorological scenarios for high ozone production rate such as no or light wind under strong solar radiation,

70   O_3 pollution episodes have been repeatedly recorded. The mixing ratio of O_3 (8-hour maximum average) could reach over 100

71   ppbv, doubling or tripling its background values. Photochemical production reactions of O_3 mainly involve volatile organic

72   compounds (VOCs), nitrogen oxides ($NO_x = NO+NO_2$) and solar radiation (Finlayson-Pitts and Jr. Pittes, 1999; Seinfeld and

73   Pandis, 2006). NO_2 photolysis produces NO and O_3 while O_3 reacts with NO to recycle NO_2. These rapidly cycling processes

74   (within minutes) are defined as the Leighton cycle. Under the photostationary-state (PSS) assumption for the Leighton cycle,

75   neither O_3 production nor loss is occurring. Production rate of O_3, referred to as $P(O_3)$, increases as peroxy radicals (HO_2+RO_2)

76   efficiently oxidize NO to produce extra NO_2 (Eq. 1). Additionally, photochemical consumption of O_3, referred to as $L(O_3)$ (Eq.

77   2), represents a considerable fraction of a comprehensive chemical budget of O_3 to offset O_3 production:

78    $$P(O_3) = k_{HO_2+NO}[HO_2][NO] + \sum_i (\alpha_i k_{RO_{2i}+NO}[RO_{2i}][NO]) \tag{1}$$

79    $$L(O_3) = f_{O(^1D)+H_2O} j_{O_3}[O_3] + k_{OH+O_3}[OH][O_3] + k_{HO_2+O_3}[HO_2][O_3] + \sum_i (k_{O_3+Alkene_i}[O_3][Alkene_i]) +$$

80    $$k_{OH+NO_2}[OH][NO_2] + L(O_3+halogens) \tag{2}$$

81    $$OPR = P(O_3) - L(O_3) \tag{3}$$

82   where $k_{RO_{2i}+NO}$ defines the rate coefficient of the reaction between a specific peroxy radical and NO. Alkyl nitrate formation

83   from molecule isomerization of [R-O-O-NO] competes with O_3 production. The yield of O_3 production is defined as α_i for a

84   specific RO_2 as it reacts with NO, while corresponding yield of alkyl nitrate is defined as $1 - \alpha_i$. $f_{O(^1D)+H_2O}$ is defined as the

85   probability of an oxygen atom, a photo-fragment of O_3 photolysis, reacting with water vapor to produce two OH radicals. OPR

86   represents the effective or net production rate of O_3.

87   NO_x and VOCs regulate the photochemical cycling of radicals and therefore OPR. Under low-NO_x conditions, bimolecular

88   reactions among peroxy radicals buffer the accumulation and chain propagation of peroxy radicals. Increasing abundance of

89   NO_x thus favors chain propagation of peroxy radicals, outcompetes bimolecular reactions among peroxy radicals and favors

90   photochemical production of O_3. Under high-NO_x conditions, chain termination reaction of NO_2 with OH radical, one major

91   route of O_3 photochemical consumption, competes with the chain propagation of peroxy radicals and photochemical production

92   of O_3. This scenario analysis reveals the nonlinear relationship between OPR and its precursor of NO_x (Cazorla et al., 2012;

93   Guo et al., 2021). The role of VOCs in O_3 production and the common sources of both VOCs and NO_x in some areas further

94   complicate the OPR-NO_x relationship and its temporal-spatial variability (Schroeder et al., 2017). High time resolution

95   characterization of OPR in the specific atmosphere of concern will be essentially helpful to characterize OPR-NO_x relationship

96   and its environmental variability.

97   In view of aforementioned expressions, Obs-OPR or Mod-OPR can be obtained from the measured or model-simulated HO_2

98   and RO_2, given mixing ratio of NO is usually measured in field campaigns (Ren et al., 2003, 2013; Green et al., 2006; Kanaya,

99   2002; Griffith et al., 2015; Tan et al., 2019b). A NO_x-dependent representation of Mod-OPR was now summarized with

100   consistent and considerable underestimation in high-NO_x areas (Ren et al., 2013; Tan et al., 2019b, 2017; Whalley et al., 2018,

101   2021; Brune et al., 2016) while slightly underestimation or even possible overestimation in low-NO_x areas (Ren et al., 2003;

102   Whalley et al., 2018). For instance, Ren et al. developed an observation-prescribed box model and outputted a underestimated

103   Mod-OPR by up to one order of magnitude compared with Obs-OPR when the median NO mixing ratio reached 17 ppbv (Ren

104   et al., 2013), while overestimated Mod-OPR by 1.4–1.7 times when NO was below 1.0 ppbv was also reported (Ren et al.,

105   2003). Evidently, such observation-model discrepancy on OPR decreased our confidence for understanding both the O_3 budget

106   and policy efficiency of regional O_3 pollution control.

107   The idea of direct measurement of OPR, Mea-OPR, which dated as far back as 1971, was first proposed by Jeffries (1971).

108   The principle is based on differential O_3 signal when ambient air continuously flows into two identical and horizontally

109   oriented chambers, one of which (called reaction chamber) is enough transparent for UV and visible radiation to mimic ambient

110   photochemistry and the other one (named reference chamber) is covered or coated by UV-blocking film to filter UV to suppress

111   the O_3 photochemical production (Cazorla and Brune, 2010; Baier et al., 2015; Sadanaga et al., 2017; Sklaveniti et al., 2018).

112   As simultaneous measurements of NO_2 and O_3 (= O_x) in the reaction chamber and reference chamber can cancel out any ozone

113   difference resulting from the rapid interconversion between NO_2 and O_3 in two chambers, a differential O_x signal rather than

114   O_3 was further adopted. We refer to the twin-chamber method for direct measurement of OPR or the measurement result by

115   such method as Mea-OPR in the context.

116   Accurate and precise Mea-OPR relies on several assumptions implied from the twin-chamber measurement scheme. The

117   most important one is that photochemistry in the reaction chamber should be able to mimic the ambient condition while O_3

118   photochemistry in the reference chamber is totally suppressed. Several versions of Mea-OPR, or named MOPS in literature,

119   have been managed to mimic photochemistry in both chambers. Teflon film and quartz glass are usually adopted for the

120   chamber body to guarantee UV transmittance in the reaction chamber (Cazorla and Brune, 2010; Sadanaga et al., 2017;

121   Sklaveniti et al., 2018). Light transmittance achieves easily above 90% for either Teflon (FEP Teflon film, 0.05 mm thick) or

122   quartz tube, providing ideal UV conditions in the reaction chamber. UV blocking film is also effective in creating a "dark"

123   condition for O_3 photochemistry.

124   Another precondition for Mea-OPR is that measurement of O_x could precisely represent the differential O_x signal, ΔO_x,

125   between chambers. Measurement uncertainties in O_x might be enlarged as transferred to be the measurement uncertainties in

126   ΔO_x, thus further amplifying the measurement uncertainties of Mea-OPR in a unit of ppbv h^{-1} because the gas residence time

127   in Mea-OPR chambers is typically much shorter than 1 hour. Both insensitivity and the drift in measurement baseline of O_3

128 and NO_2 instruments contribute to the measurement uncertainties of ΔO_x (Cazorla and Brune, 2010; Baier et al., 2015). Such

129 stringent requirement in precise ΔO_x measurements requires advanced and tested measurement techniques and well trained

130 technicians to perform the measurement, which might limit the widespread deployment of Mea-OPR. Reliable and sensitive

131 measurement technique for O_3 and NO_2 might be a savior in this situation.

132   Last but not least, the chamber wall effect must be suppressed and quantified. The chamber wall effect might change the

133 abundance of O_x, which presents false signal of ΔO_x that is difficult to be decoupled from photochemical ΔO_x. The chamber

134 wall effect might also change the abundance of photochemical intermediates, leading to unwanted perturbation on O_3

135 photochemistry in the reaction chamber. Sklaveniti et al. (2018) estimated that O_3 uptake loss in their version of Mea-OPR

136 would lead to false Mea-OPR signal of ~20 ppbv h^{-1} assuming ambient O_3 to be 50 ppbv. It was also found that HONO

137 production in uptake experiment of NO_2 on quartz chamber and Teflon chamber can reach up to tens of ppbv h^{-1} under

138 irradiated conditions, which would lead to an overestimation of Mea-OPR by approximately 27% on average (Sklaveniti et

139 al., 2018) or Mea-OPR error of around 10 ppbv h^{-1} (Baier et al., 2015). Effective design to suppress the wall effect is, therefore,

140 the key to ensure the data quality of Mea-OPR. Previous designs are devoted to keeping the air in plug flow motion and a

141 small-diameter (14.0–17.8 cm) chamber is usually chosen for it is easier to manipulate (Cazorla and Brune, 2010; Baier et al.,

142 2015; Sadanaga et al., 2017; Sklaveniti et al., 2018). However, a small diameter works against the wall effect suppression. The

143 S/V ratio was decreased by 20% by employing a larger chamber volume (26.9 L) in the second version of Mea-OPR (Baier et

144 al., 2015), relative to the first generation (11.3 L) (Cazorla and Brune, 2010). Referring to the uptake coefficient calculation

145 formula (Eq. 4), a 20% decrease of S/V will result in a 20% reduction in false Mea-OPR signal due to uptake loss of O_3 for a

146 given uptake coefficient and O_3 abundance. Previous research has also confirmed less O_x loss on Teflon wall surface (Sadanaga

147 et al., 2017) than on quartz surface (Sklaveniti et al., 2018). Sadanaga et al. (2017) first managed to coat the inner wall surface

148 of the quartz chamber with transparent Teflon and effectively reduced the wall effect.

149   $\gamma_{O_3} = \dfrac{4 \times \Delta O_{3,\,uptake}}{O_{3,\,amb} \times \omega_{O3} \times \tau \times S/V}$ (4)

150   To date, these effective designs have not yet been integrated and evaluated in a state-of-the-art version of Mea-OPR. In this

151 article, we will present our construction of a state-of-the-art Mea-OPR and condition experiments to characterize this Mea-

152 OPR. Later, the employment of Mea-OPR system in Beijing, a megacity in China, provides further validation of it.

153 **2 Experimental section**

154 **2.1 Construction of state-of-the-art Mea-OPR**

155   The schematic of our Mea-OPR is shown in Fig. S1. The quartz chamber inner wall was coated with the transparent Teflon.

156 It was chosen over the Teflon film chamber for Teflon film chamber showed its weakness in working in high wind velocity

157 conditions. The quartz chamber and the Teflon coating together presented an ideal transmittance (> 88%) for both UV and

158   visible light (Fig. S2). The difference in $j(O^1D)$ between the ambient and the reaction chamber calculated by measured solar

159   flux (Metcon CCD-Spectrograph) in Beijing winter was within 4% (Table S1). UV filter was adopted for the reference chamber

160   (transmittance for UV was 0, Fig. S3) and enabled small temperature and RH differences in both chambers (Fig. S4).

161   Parallel and accurate measurements of ΔO_x were supported by two identical sets of O_3 analyzer (Thermo Scientific, Model

162   49i, LOD: 1.0 ppbv) and NO_2 analyzer (Los Gatos Research, Inc., Model 911-0009, LOD: 50 pptv). To calculate the wall loss

163   of O_x in both chambers in real time, another set of O_3 analyzer (Thermo Scientific, Model 49i, LOD: 1.0 ppbv) and homemade

164   iBBCES-NO_2 instrument (AIOFM, LOD: 168 pptv; 30 min background shifted: 100 pptv) (Fang et al., 2017) were sampling

165   the ambient air. The system was running with a duty cycle in a 23 h plus 1 h, which included 1 h instrument alignment as all

166   instruments shifted to the ambient sampling line at midnight. The purpose of the instrument alignment was to check the

167   working status of the measurements on a daily base, rather than data correction. ΔO_x up to 1 ppbv in a 1 h alignment reminded

168   of instrument calibration and maintenance, which were otherwise conducted on a weekly basis. Under the working protocol,

169   the system performed stably in a 1-month measurement duty from February 5 to March 12, 2022. Multiple calibrations

170   suggested the instrument response shifted within ±0.4% and ±1.9% for O_3 and NO_2, respectively, in this period (Table S2).

171   The instrument alignment experiment suggested that nigttime ΔO_x was 0.07 (±0.26) ppbv, within the instrument detection

172   limits (Fig. S5).

173   Our Mea-OPR development put emphasis on wall effect management. The diameter of our Mea-OPR was 41 cm, which

174   produced a S/V ratio that was 1.8 fold less than the lowest value ever published in the literature (Cazorla and Brune, 2010;

175   Baier et al., 2015). This reduced the O_3 wall effect by 1.8 folds even though the same uptake coefficient of O_3 was taken into

176   consideration (Eq. 4), and so did for wall effect of other species, such as NO_2 and HONO. Larger diameter of our Mea-OPR

177   also gave the flexibility of the working flow rate, which spanned from 5 to 20 L min^{-1} while enabling multiple sampling

178   instruments equipped and a residence time of up to 30 min in a plug flow mode (Fig. S1). Another key design to suppress the

179   wall effect was the transparent Teflon coating, which was essential for accurate Mea-OPR by reducing the uptake coefficient

180   of O_3 from 10^{-8} on quartz wall (Sklaveniti et al., 2018) to 10^{-9} on Teflon coating wall under dark conditions.

181   Mea-OPR can be calculated in Eq. (5), wherein ΔNO_2 and ΔO_3 are the difference values of NO_2 and O_3 between both

182   chambers, respectively. τ is the mean gas residence time in chambers (Fig. S6). γ is the uptake coefficient of O_3 in the

183   chamber. ω represents the mean molecular velocity of O_3 in m s^{-1}. D is the diameter of chambers in m. $O_{3,\,amb}$ represents

184   the ambient O_3 concentration in ppbv. φ_{trans} is the ratio of in-chamber $j(O^1D)$ to ambient $j(O^1D)$ as determined by the UV

185   transmittance of Mea-OPR system. $\varphi_{\Delta HONO\ or\ \Delta NOx}$ is the ratio of OPR in the reaction chamber to that in the ambient owing to

186   the presence of $\Delta HONO$ or ΔNO_x between the reaction chamber and the ambient.

187    $$\text{Mea-OPR} = \left(\frac{\Delta NO_2 + \Delta O_3}{\tau} + \frac{(\gamma_{Rea} \cdot \omega_{Rea} - \gamma_{Ref} \cdot \omega_{Ref}) \cdot O_{3,\,amb}}{D} \right) \cdot \frac{1}{\varphi_{trans} \cdot \varphi_{\Delta HONO\ or\ \Delta NOx}} \qquad (5)$$

188 **2.2 Condition experiments to characterize wall effect**

189   As Mea-OPR was sampling the ambient air, O_3 wall loss and photochemical production were occurring simultaneously and,
190 thus, cannot be decoupled from each other. A condition experiment of zero-NO_x-and-zero-VOCs (referred to as zero-NO_x-
191 and-high-O_3 experiment) was designed and, thus, zero OPR was assumed. High O_3 control (also referred to as ambient O_3 for
192 simplicity) in zero-NO_x-and-high-O_3 experiment favored measurement of O_3 wall losses directly in both chambers on 6 March,
193 2022. In addition, HONO production from NO_2 uptake (Eq. 6) on the Teflon film and quartz surface have been proposed by
194 Baier et al. (2015) and Sklaveniti et al. (2018) as a potential perturbation on photochemical production of O_3 in the reaction
195 chamber. To obtain differential NO_x and HONO signals in chambers relative to the ambient, additional measurements of
196 HONO in the chambers and in the ambient were equipped in a 1-week HONO production experiment as Mea-OPR was
197 deployed in 11–18 February, 2022. The above condition experiments to characterize wall effect were described in detail in the
198 Supplement (S2.6).

199    $2NO_2 + H_2O \text{ (ads)} \rightarrow HONO + HNO_3$ (6)

200 **2.3 Field application of Mea-OPR**

201   Our Mea-OPR system was deployed on the top floor of an academic building on the campus of Peking University (39°59′23″
202 N, 116°18′25″ E). The observatory as a typical urban and polluted site in Beijing City, China, was impacted by considerable
203 fresh, anthropogenic emissions in the surroundings, such as the 4th ring-road traffic emission. More details about this site were
204 also described elsewhere (Guo et al., 2010; Tang et al., 2018). Notably, the measurement period coincided with the Beijing
205 2022 Winter Olympic Games from 4 to 20 February, when the Municipal Government of Beijing implemented a package of
206 factory and transportation controls to improve air quality. Owing to the aggressive control measures and favorable
207 meteorological conditions, no haze events and substantial reductions in gas pollutant concentrations were observed (Guo et
208 al., 2023; Liu et al., 2022). Therefore, the air pollution conditions during this period can be regarded as relatively clean
209 compared to those polluted episodes in the same period of other years.

210 **3 Results and discussion**

211 **3.1 O_3 uptake evaluation**

212   A zero-NO_x-and-high-O_3 experiment was conducted for directly measuring the O_3 wall loss in both chambers with little
213 perturbation from O_3 photochemical production in chambers. As shown in Fig. 1a, evident O_3 wall loss ($\Delta O_{3, \text{raw}} = O_3$ in the
214 ambient $- O_3$ in the chamber) were observed and higher O_3 wall loss was observed for the reaction chamber ($\Delta O_{3, \text{raw}} = 7.7$
215 ppbv) relative to the reference chamber ($\Delta O_{3, \text{raw}} = 2.3$ ppbv) at noon. The ambient O_3 control was measured at approximately
216 113.0 ppbv just before entering chambers. NO_x concentration was measured around 0.03–1.05 ppbv to double-check the low
217 level of NO_x in the control experiment. A slight increase in NO_x from the morning to the noon was accompanied with increasing

218   $j(O^1D)$, which might be attributed to the previously-identified unknown source of HONO and NO_x in Teflon chamber (Zhou

219   et al., 2003). The unknown chamber source of HONO was also confirmed later during the 1-week HONO production

220   experiment (see below). The MCM model was conducted to calculate O_3 production in chambers. NO_x and CO were both

221   major prescribed chemical parameters. At noon, the corresponding O_3 production in the reaction chamber, $\Delta O_{3, photochemistry}$,

222   was found to be 2.7 ppbv in the residence time of 20 min (Fig. S7), which comprises 35% of the $\Delta O_{3, raw}$ for the reaction

223   chamber. O_3 production was negligible in the reference chamber at noon because stray light in the reference chamber was too

224   weak to be meaningful for O_3 photochemistry.

225   After eliminating the photochemical contribution, $\Delta O_{3, uptake}$ (= $\Delta O_{3, raw} - \Delta O_{3, photochemistry}$) was obtained and the uptake

226   coefficient of O_3 on chambers could be calculated according to Eq. (4). The uptake coefficient from a typical value of $7.11 \times$

227   10^{-8} on quartz wall (Sklaveniti et al., 2018) (Table S3) was successfully reduced to the present average value of 8.12×10^{-9}

228   on the transparent Teflon coating under dark conditions. Under typical working conditions of Mea-OPR, O_3 uptake loss

229   contributes to a false Mea-OPR signal of 20.3 ppbv h^{-1} at uptake coefficient of 7.11×10^{-8} and S/V ratio of 18 m^{-1} (the least

230   in the literature), relative to a false Mea-OPR signal of 1.29 ppbv h^{-1} at uptake coefficient of 8.12×10^{-9} and S/V ratio of 9.76

231   m^{-1} in our Mea-OPR, assuming ambient O_3 concentration of 50 ppbv. This calculation suggests the essential success in wall

232   effect suppression by our strategy, i.e., to minimize chamber S/V ratio and uptake coefficient of O_3 on the chamber wall, for

233   assuring the data quality of Mea-OPR.

234   During the daytime, UV-dependent γ was observed and inferred a photo-enhanced uptake of O_3 of up to 8.98×10^{-8} at noon,

235   nearly one order of magnitude higher relative to 8.12×10^{-9} at night (Fig. 1b). Low uptake coefficient of 5.17×10^{-9} under

236   dark condition was observed for Teflon surface due to its inert nature (Sadanaga et al., 2017). However, photosensitization

237   reactions of O_3 on organic coating was observed with an uptake coefficient in the range of 10^{-6}–10^{-5} under near-UV and visible

238   irradiation relative to 10^{-7}–10^{-6} in the dark (Styler et al., 2009; D'Anna et al., 2009). This suggested that the aerosol particles

239   deposited on the inner wall surface might substantially contribute to the photo-enhanced wall loss of O_3. A routine water flush

240   cleaning and UV-photochemical-aging cleaning of both chambers were then scheduled after occurrence of heavy pollution

241   episodes ($PM_{2.5} > 80$ μg cm^{-3}) (Juda-Rezler et al., 2020). RH might modify aerosol phase state and thus was another parameter

242   affecting the uptake coefficient on aerosol particles and apparent wall loss of O_3. The daytime RH was typically below 50%,

243   approximately the threshold RH of particle phase shift in the city of Beijing (Liu et al., 2016). A relatively stable γ at low RH

244   was also observed. The daytime γ was then expressed as a function of merely $j(O^1D)$, not considering the complex influence

245   from RH variation below 50% (Fig. 1c). An increasing γ as a function of RH for the nighttime was summarized, with a

246   threshold RH of *ca.* 60% (Fig. 1d).
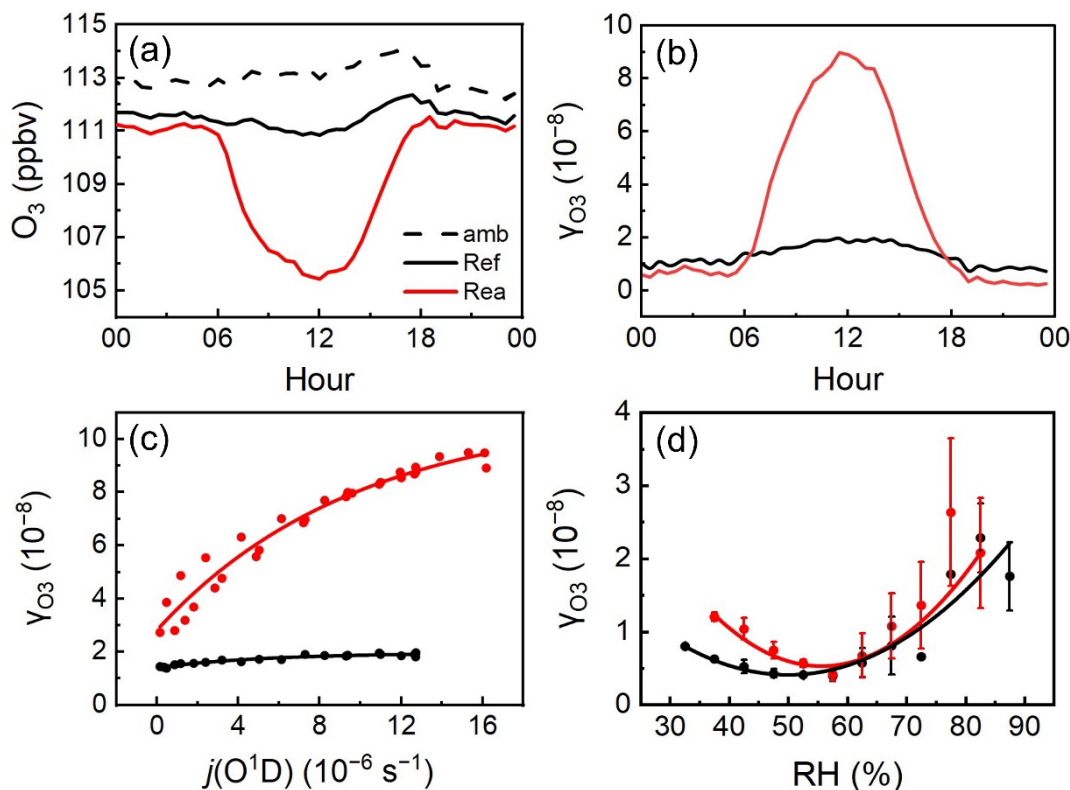
Figure 1: Results of condition experiment designed to measure O₃ wall loss. (a) O₃ concentrations in the ambient (approximately 113.0 ppbv) and in both chambers as zero-NOₓ-and-high-O₃ air was introduced to both chambers; (b) Calculated half-hour resolution uptake coefficient (γ) of O₃ in both chambers; (c) Fitted exponential relationship between γ and $j(O^1D)$ in daytime, i.e., $j(O^1D) > 1 \times 10^{-7}$ s⁻¹ (R² = 0.93 and 0.96, respectively); (d) Fitted polynomial relationship between γ and RH during night, i.e., $j(O^1D) < 1 \times 10^{-7}$ s⁻¹ (R² = 0.82 and 0.82, respectively). Error bar represents standard deviation of γ in each RH interval of 5%. Fitting method is ordinary least squares estimation.

Sklaveniti et al. (2018) also suspected photo-enhanced O₃ uptake in the reaction chamber as a major measurement interference for their Mea-OPR system utilizing quartz wall without Teflon coating. However, no quantification and correction of Mea-OPR interference from the O₃ uptake was suggested. The $j(O^1D)$-dependent γ for the daytime and RH-dependent γ for the nighttime as determined in our control experiments provided the first reliable correction for Mea-OPR (Eqs. 7–10). For the correction, O₃ concentrations measured in the ambient could be used to calculate the $\Delta O_{3,\ uptake}$ (Eq. 4). After multiple control experiments (not shown), we could also assume the uptake coefficient of O₃ being stable between two adjacent control experiments.

$$\gamma_{Ref} = -5.53 \times 10^{-9} \times \exp\left(-\frac{j(O^1D)}{5.41 \times 10^{-6}}\right) + 1.96 \times 10^{-8} \tag{7}$$

$$\gamma_{Rea} = -8.21 \times 10^{-8} \times \exp\left(-\frac{j(O^1D)}{9.76 \times 10^{-6}}\right) + 1.10 \times 10^{-7} \tag{8}$$

$$\gamma_{Ref} = 1.28 \times 10^{-11} \times RH^2 - 1.28 \times 10^{-9} \times RH + 3.60 \times 10^{-8} \tag{9}$$

9

264     $\gamma_{\text{Rea}} = 2.37 \times 10^{-11} \times RH^2 - 2.56 \times 10^{-9} \times RH + 7.50 \times 10^{-8}$ (10)

### 3.2 In-chamber HONO production evaluation

266   In the 1-week HONO production experiment, ΔNO_x (= NO_x in the ambient − NO_x in the chamber) showed no obvious
267   diurnal variation, with an average of 1.01 and 0.77 ppbv in the reaction and reference chamber, respectively (Fig. 2a). Based
268   on Eq. (S3), the average uptake coefficient of NO_2 in the reaction and reference chamber were calculated as 8.66×10^{-8} and
269   6.43×10^{-8}, respectively. Despite of considerable uptake coefficient of NO_2, compared with that of O_3, much lower NO_2 level
270   (12.9 ppbv) relative to O_3 inferred negligible wall loss of NO_2, which was transferred to *ca.* 1.79 ppbv h^{-1} false signal of Mea-
271   OPR at most during the 1-week HONO production experiment. The perturbation on O_3 photochemistry in the reaction chamber
272   by such ΔNO_x was evaluated by MCM model to be negligible due to the insensitive response of O_3 photochemistry to NO_x
273   abundance in the range around 10 ppbv.

274   Uptake loss during the nighttime and production of HONO during the daytime in both chambers were spotted (Fig. 2b).
275   Nighttime loss of HONO on the wall surface, as observed in the lower HONO in both chambers relative to the ambient HONO
276   ($\Delta HONO$ = −0.22 ppbv on average for the reaction chamber), was not suspected even assuming that uptake loss of NO_2 and
277   heterogenous production of HONO were negligible (Sadanaga et al., 2017). However, Sklaveniti et al. (2018)   reported HONO
278   production rate of up to 9 ppbv h^{-1} in controlled ambient concentration of NO_2 under dark condition. HONO uptake on
279   deliquescent aerosol particles at night might account for the HONO loss here (Ren et al., 2020). RH in the reaction chamber
280   scattered at approximately 61% (±14%) and was much higher than the ambient air of 36% (±14%) during the nighttime, which
281   might lead to deliquescence of deposited aerosol particles on the wall surface. As the temperature rose and RH dropped in the
282   early morning, uptake loss of HONO on the wall surface was diminishing. Further decrease in the zenith angle even led to
283   production or release of HONO in both chambers, resulting in a higher HONO concentration in both chambers relative to the
284   ambient air during the daytime ($\Delta HONO$ = 0.09 ppbv on average for the reaction chamber). Either heterogeneous uptake of
285   NO_2 or unknown temperature-related or UV-related chamber source of HONO or releasing of nighttime uptaken HONO might
286   account for the daytime $\Delta HONO$ in chambers. Daytime $\Delta HONO$ herein appeared to be less than previous reports in laboratory
287   condition (Sklaveniti et al., 2018) and in the ambient of Houston (Baier et al., 2015). Both the inert surface coating and less
288   abundant NO_2 in 1-week HONO production experiment might justify the result.

289   While the small ΔNO_2 and $\Delta HONO$ contribute slightly to the measurement uncertainty of ΔO_x, daytime HONO production
290   in the reaction chamber might perturb the O_3 photochemistry therein and challenge the mimic of O_3 photochemistry by the
291   reaction chamber (Baier et al., 2015; Sklaveniti et al., 2018). We then evaluated the O_3 production difference in the reaction
292   chamber relative to the ambient air. Since the radical budget is closely related to O_3 chemistry (Tan et al., 2018a; Ma et al.,
293   2022), the primary RO_x source budget and O_3 production in the reaction chamber and the ambient air were calculated and
294   compared, based on the MCM models prescribed with HONO in the ambient air and the reaction chamber, respectively. When
295   the HONO difference between the reaction chamber and the ambient air was maximum in the daytime, HONO photolysis
296   comprised 22.2% of the total primary RO_x source budget for the ambient air, while constituted 28.2% of the total primary RO_x

Atmospheric
Measurement
Techniques

EGU

Open Access

Discussions

297   source budget for the reaction chamber. The overall primary RO_x source budget was at most 8.1% higher in the reaction

298   chamber than in the ambient air, which revealed that $\Delta HONO$ considerably perturbed the RO_x source budget owing to the

299   considerable contribution from HONO photolysis. Furthermore, O_3 production enhancement owing to HONO production in

300   the reaction chamber, relative to the ambient air, was calculated as 4.5% at most during the 1-week HONO production

301   experiment (Fig. 2c). It could be seen that although the HONO production in the reaction chamber significantly increased the

302   RO_x source budget and promoted the O_3 production, it might also increase the sink of O_3 accordingly, and in general, it had

303   little effect on the net O_3 production. While in less polluted environments, the perturbation of HONO on O_3 photochemistry

304   was assumed to be less and, therefore, negligible. Currently, NO_2 uptake and HONO production correction are not applied for

305   our Mea-OPR.
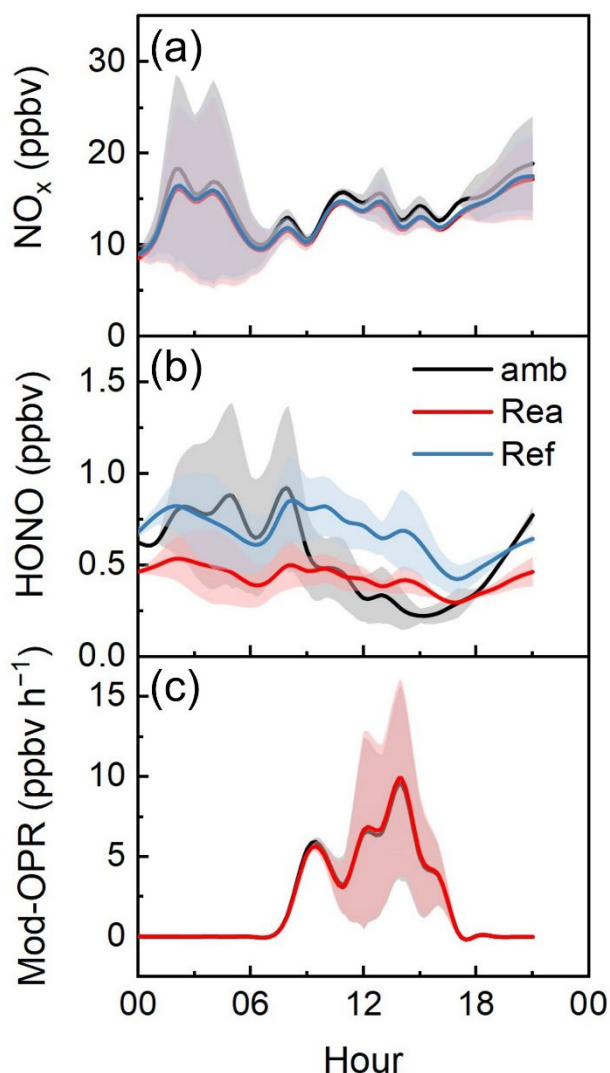
306

307   **Figure 2: Diurnal variation of average hourly (a) NO_x and (b) HONO concentrations in ambient air and both chambers. (c)**

308   **Comparison of O_3 production simulation as prescribed with HONO in ambient air and reaction chamber during condition**

309   **experiment of HONO production. Shaded areas represent 1SD variation of NO$_x$, HONO, and OPR for the 1-week HONO production**
310   **experiment.**

3.3 Uncertainty evaluation for Mea-OPR

312   The detection limit of 2.8 ppbv h^{-1} of our Mea-OPR was determined by three times the standard deviation of Mea-OPR
313   during nighttime (21:00–04:00) when OPR was supposed to be near null. Currently, tropospheric OPR in remote and rural
314   areas is believed to be lower than 5 ppbv h^{-1} (Kanaya, 2002; Xue et al., 2013; Bozem et al., 2017). In polluted regions, OPR
315   can be up to tens of ppbv h^{-1} (Baier et al., 2015; Kleinman, 2005; Xue et al., 2021; Tan et al., 2021; Whalley et al., 2021; Zhou
316   et al., 2014; Cazorla et al., 2012). Hence, our system is sensitive enough to detect OPR in polluted urban sites, but might not
317   be so in the clean remote sites.

318   The uncertainties of Mea-OPR arise from UV transmittance of the chamber wall, measurements of gas residence time and
319   ΔO_x, and correction from O$_3$ and NO$_2$ wall loss, or HONO production in the reaction chamber (Table S4). Assuming a linear
320   relationship among Mea-OPR and $j(\mathrm{O^1D})$, reduction in $j(\mathrm{O^1D})$ in the reaction chamber and stray light in the reference chamber
321   contribute to uncertainties of −4% and −5%, respectively (Table S1). The measurement uncertainty of gas residence time is
322   evaluated from the multiple residence time measurements to be better than ±0.45%. Evaluated from 1-hour consistency
323   measurements every night, the measurement uncertainties for $\Delta \mathrm{NO_2}$ and $\Delta \mathrm{O_3}$ are ±3.8% and ±1.1%, respectively. Higher
324   uncertainties were found at low levels of NO$_x$ or O$_3$, which suggests that continuous improvement in ΔO_x measurement
325   precision will benefit our measurement. The largest uncertainty of Mea-OPR comes from the wall effect of O$_3$ and in our case
326   the wall effect correction of O$_3$. The wall effect correction functions of O$_3$ indicate a higher wall effect of O$_3$ as $[\mathrm{O_3}] \times j(\mathrm{O^1D})$
327   is higher. As a strong O$_3$ production is also presumed when $[\mathrm{O_3}] \times j(\mathrm{O^1D})$ is higher, the wall effect correction of O$_3$ does not
328   indicate lower measurement quality in strong O$_3$ production scenario. The uncertainties of the fitted O$_3$ uptake coefficient in
329   both chambers (Eqs. 7–10) are ±4.4% and ±23%, respectively. Wall effect of HONO contributes to an uncertainty of +4.5%,
330   evaluated from the condition experiment. The total uncertainty of our Mea-OPR can be obtained by error propagation as
331   described in detail in the Supplement (S2.7). As shown in Fig. S8, the total uncertainty of the Mea-OPR system decreases with
332   the increase of Mea-OPR. When Mea-OPR is above the detection limit of 2.8 ppbv h^{-1}, the uncertainty of Mea-OPR system is
333   stable and low at an average value of ±27%. In addition, when the O$_3$ uptake coefficient decreases, the uncertainty of Mea-
334   OPR also clearly reduces, which further indicates the importance of reducing O$_x$ uptake in the chambers for the accurate
335   measurement of Mea-OPR.

3.4 Field application in urban site of Beijing

337   The mean diurnal profile of ambient $j(\mathrm{O^1D})$, NO, NO$_2$, O$_3$ and Mea-OPR during the Beijing 2022 Winter Olympic Games
338   are shown in Fig. 3. NO$_x$ levels ranged from approximately 0.5 to 112.8 ppbv, with an averaged value about 18.2 (±16.7) ppbv,
339   which was similar to that observed at the suburban site (Huairou Station) of Beijing from January to March, 2016 (Tan et al.,
340   2018b), but much lower than our measurement of 32.0 (±22.4) ppbv in the winter of 2021 (not shown). Specific pollution

341 control measures for the Beijing 2022 Winter Olympic Games reconcile such a discrepancy. The maximum daily concentration

342 of NO_2 climbed to 26.6 ppbv during the end of our field campaign, which was normal as compared to the winter 2021

343 campaign. O_3 concentration showed afternoon (14:00–16:00) maxima and early morning (6:00–8:00) minima (Fig. 3b), the

344 former of which was a typical feature of photochemical production. The O_3 levels varied from 1.2 to 90.5 ppbv in the daytime,

345 and the mean and median values were approximately 34.4 (±13.9) ppbv and 36.6 ppbv, respectively. In fact, O_3 titration by

346 NO in this urban site was apparent during the morning/afternoon rush hours, but less evident at noon as it was seen from the

347 NO/NO_2 ratio during rush hours (0.20) and noon (0.46), in comparison with the photo-steady-state ratio of 0.14 and 0.44,

348 respectively. Considering the O_3 titration, the urban diurnal O_x concentration was 43.5 (±3.1) ppbv, higher than the regional

349 background of 38.0 ppbv (Xu et al., 2020), suggesting the urban area was still the regional source of O_3 pollution. Noontime

350 $j(O^1D)$ peaked at approximately 1.0×10^{-5} s^{-1} on average (Fig. 3c), less than half of the value during the summer (2.6×10^{-5}

351 s^{-1}) (Tan et al., 2019a). Mea-OPR showed similar diurnal variation to $j(O^1D)$. Mean Mea-OPR peaked at 7.4 ppbv h^{-1} at around

352 12:30 (Fig. 3c), which was smaller than the O_3 production peak of 20 ppbv h^{-1} measured using the Obs-OPR method in summer

353 at the PKU urban site (Tan et al., 2019a). The nighttime Mea-OPR approached zero as it was also expected from the low levels

354 of O_3, NO_3, and RO_2 (not shown), accompanied with a nighttime NO of 2.3 ppbv. Therefore, such high Mea-OPR confirmed

355 active O_3 photochemistry and that urban Beijing was still a regional source of O_3 pollution even though the pollution control

356 policy was implemented during the Winter Olympic Games.
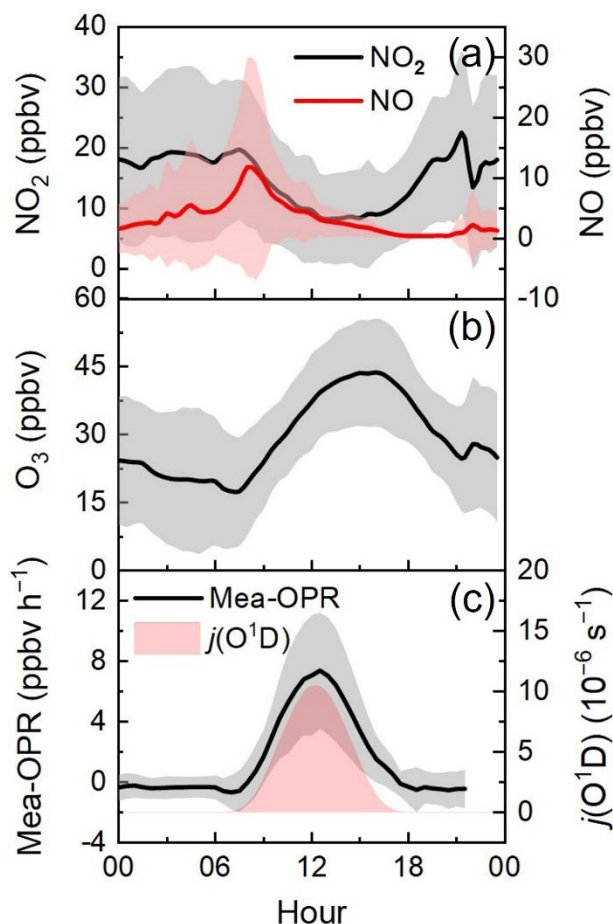
Figure 3: Mean diel profiles of (a) NO and NO2, (b) O3, and (c) Mea-OPR and $j(O^1D)$ at PKU urban site during field campaign. Shaded areas represent 1SD variation of measurement parameters.

A linear relationship was established for Mea-OPR *versus* $j(O^1D)$, but an atypical relationship was established for Mea-OPR *versus* NO from the Gaussian-shaped ones (Fig. 4) (Whalley et al., 2021; Cazorla et al., 2012). The linear relationship between Mea-OPR and $j(O^1D)$ justified that our Mea-OPR measurement captured its photochemical pattern well. The fitting slope of the Mea-OPR *versus* $j(O^1D)$ plot was 6.1×10^5 ppbv h^{-1} s^{-1}. Compared with a study of Xue et al. (2013) in a global background site of Waliguan, the fitting slope in this study was higher, which might suggest the relatively active nature of O3 photochemistry in winter in Beijing. With relatively high NOx level and assumed VOCs-limited regime for O3 production in Beijing, O3 photochemistry was expected to be suppressed under high-NOx conditions. However, an atypical relationship was observed here, as also being validated in Obs-OPR *versus* NO plot (Whalley et al., 2021; Cazorla et al., 2012). The continuous increase in OPR as NOx increased even in high-NOx conditions might have accounted for the active O3 photochemistry in urban Beijing. Detailed reasons for such atypical relationship are not yet clear, but our Mea-OPR shows its promising capacity to capture both expected and atypical patterns of O3 photochemistry alongside the change of $j(O^1D)$ and NO.

14

Atmospheric
Measurement
Techniques

Discussions

371
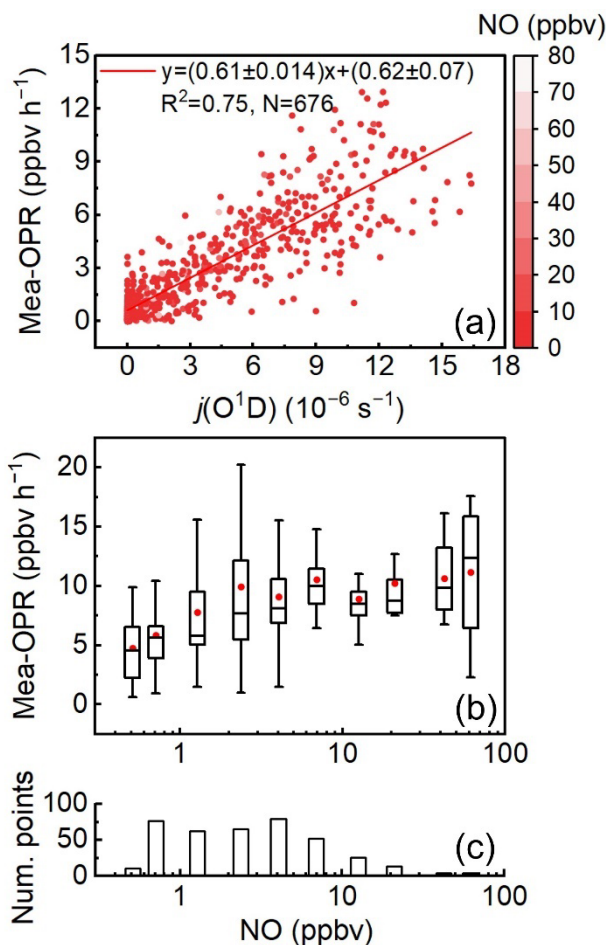
Figure 4: Plot of Mea-OPR against (a) $j(O^1D)$ and (b) NO for daytime conditions ($j(O^1D) > 10^{-7}$ s^{-1}) during field campaign. The interval of NO bin is $\Delta\ln(NO) = 0.57$ ppbv. Panel (c) shows number of datapoints included in each NO interval.

4 Conclusions

Accurate quantification of OPR is an important premise to effective O_3 pollution control strategy and to control the adverse effects of O_3 pollution on human health and climate. Previous studies have shown discrepancies between Obs-OPR and Mod-OPR, which indicates that our understanding of O_3 photochemistry is yet-perfect. Direct measurement of OPR using a twin-chamber system (Mea-OPR) could provide an accurate measurement of OPR, shining light on the emerging conceptual framework of O_3 photochemistry. In this work, we reported an optimized system for direct measurement of ozone production rate, Mea-OPR, and its employment at an urban site of Beijing. Our study optimized the chamber design in several ways, i.e., considerably increased the chamber volume and, thus, broadened the optional range of flow rate; employment of a large chamber diameter and the Teflon coating on the inner wall of the chamber to suppress the wall effect. We minimized the chamber surface area to volume ratio to 9.8 m^{-1} and the dark uptake coefficient of O_3 to the order of 10^{-9}. In addition, photo-

Atmospheric
Measurement
Techniques
Discussions

384 enhanced uptake of O_3 on deposited particulate matter was found to be the major error source of Mea-OPR. Condition
385 experiments further revealed a photo-enhanced O_3 uptake and recommended a quantitative correction. We finally characterized
386 a detection limit of 2.8 ppbv h^{-1} and a measurement uncertainty of $\pm$27%, which suggests that Mea-OPR is sensitive enough
387 to measure OPR in urban or suburban environments. Application of this system in urban Beijing during the Winter Olympic
388 Games recorded a noontime Mea-OPR of 7.4 ($\pm$3.8) ppbv h^{-1} and Mea-OPR *versus* j(O^{1}D) slope of 6.1 $\times$ 10^5 ppbv h^{-1} s^{-1},
389 which indicates fairly active O_3 photochemistry despite the pollution control policy. The fairly active O_3 photochemistry was
390 mainly assisted by a high abundance of VOCs and NO$_x$, atypically high Mea-OPR even under high-NO$_x$ conditions, but
391 mediated by relatively weak ultraviolet radiation.

393 *Data availability.* Contact the corresponding author for data.

395 *Supplement.* The following file is available free of charge. Optimizing a twin-chamber system for direct ozone production rate
396 measurement_ SI

398 *Author Contributions.* Y.W. and C.Y. built the Mea-OPR system, Y.C. and S.C. conducted the condition experiments,
399 interpreted the data, and wrote the manuscript with revision mainly from Y.W., C.Y., and other authors. Y.W., Y.C., and S.C.
400 contributed equally to this work and should be considered co-first authors. All authors have given approval to the final version
401 of the manuscript.

409
410
411
412
413
414
415
416
417

Atmospheric
Measurement
Techniques
Discussions

418 **References**

419 Ashmore, M. R.: Assessing the future global impacts of ozone on vegetation, Plant. Cell. Environ., 28, 949–964,
420   https://doi.org/10.1111/J.1365-3040.2005.01341.X, 2005.

421 Baier, B. C., Brune, W. H., Lefer, B. L., Miller, D. O., and Martins, D. K.: Direct ozone production rate measurements and
422   their use in assessing ozone source and receptor regions for Houston in 2013, Atmos. Environ., 114, 83–91,
423   https://doi.org/10/gnxf26, 2015.

424 Bozem, H., Butler, T. M., Lawrence, M. G., Harder, H., Martinez, M., Kubistin, D., Lelieveld, J., and Fischer, H.: Chemical
425   processes related to net ozone tendencies in the free troposphere, Atmos. Chem. Phys., 17, 10565–10582,
426   https://doi.org/10.5194/acp-17-10565-2017, 2017.

427 Brune, W. H., Baier, B. C., Thomas, J., Ren, X., Cohen, R. C., Pusede, S. E., Browne, E. C., Goldstein, A. H., Gentner, D. R.,
428   Keutsch, F. N., Thornton, J. A., Harrold, S., Lopez-Hilfiker, F. D., and Wennberg, P. O.: Ozone production chemistry in the
429   presence of urban plumes, Faraday Discuss., 189, 169–189, https://doi.org/10.1039/C5FD00204D, 2016.

430 Cazorla, M. and Brune, W. H.: Measurement of Ozone Production Sensor, Atmos. Meas. Tech., 3, 545–555,
431   https://doi.org/10.5194/amt-3-545-2010, 2010.

432 Cazorla, M., Brune, W. H., Ren, X., and Lefer, B.: Direct measurement of ozone production rates in Houston in 2009 and
433   comparison with two estimation methods, Atmos. Chem. Phys., 12, 1203–1212, https://doi.org/10.5194/acp-12-1203-2012,
434   2012.

435 D'Anna, B., Jammoul, A., George, C., Stemmler, K., Fahrni, S., Ammann, M., and Wisthaler, A.: Light-induced ozone
436   depletion by humic acid films and submicron aerosol particles, J. Geophys. Res., 114, D12301,
437   https://doi.org/10.1029/2008JD011237, 2009.

438 Fang, B., Zhao, W., Xu, X., Zhou, J., Ma, X., Wang, S., Zhang, W., Venables, D. S., and Chen, W.: Portable broadband cavity-
439   enhanced spectrometer utilizing Kalman filtering: application to real-time, in situ monitoring of glyoxal and nitrogen
440   dioxide, Opt. Express, 25, 26910, https://doi.org/10.1364/OE.25.026910, 2017.

441 Finlayson-Pitts, B. J. and Jr. Pittes, J. N.: Chemistry of the Upper and Lower Atmosphere, academic press, San Diego,
442   California, 1999.

443 Forster, P., Ramaswamy, V., Artaxo, P., Berntsen, T., and Dorland, R. V.: Changes in atmospheric constituents and in radiative
444   forcing, in: Climate Change 2007: The Physical Science Basis. Contribution of Working Group I to the Fourth Assessment
445   Report of the Intergovernmental Panel on Climate Change, Cambridge University Press, Cambridge, UK and New York,
446   USA, 2007.

447 Green, T. J., Reeves, C. E., Fleming, Z. L., Brough, N., Rickard, A. R., Bandy, B. J., Monks, P. S., and Penkett, S. A.: An
448   improved dual channel PERCA instrument for atmospheric measurements of peroxy radicals, J. Environ. Monit., 8, 530,
449   https://doi.org/10/d95fhs, 2006.

450   Griffith, S. M., Huang, X. H. H., Louie, P. K. K., and Yu, J. Z.: Characterizing the thermodynamic and chemical composition

451   factors controlling PM$_{2.5}$ nitrate: Insights gained from two years of online measurements in Hong Kong, Atmos. Environ.,

452   122, 864–875, https://doi.org/10.1016/j.atmosenv.2015.02.009, 2015.

453   Guo, F., Bui, A. A. T., Schulze, B. C., Yoon, S., Shrestha, S., Wallace, H. W., Sakai, Y., Actkinson, B. W., Erickson, M. H.,

454   Alvarez, S., Sheesley, R., Usenko, S., Flynn, J., and Griffin, R. J.: Urban core-downwind differences and relationships

455   related to ozone production in a major urban area in Texas, Atmos. Environ., 262, 118624,

456   https://doi.org/10.1016/j.atmosenv.2021.118624, 2021.

457   Guo, S., Hu, M., Wang, Z. B., Slanina, J., and Zhao, Y. L.: Size-resolved aerosol water-soluble ionic compositions in the

458   summer of Beijing: implication of regional secondary formation, Atmos. Chem. Phys., 10, 947–959,

459   https://doi.org/10.5194/acp-10-947-2010, 2010.

460   Guo, Y., Deng, C., Ovaska, A., Zheng, F., Hua, C., Zhan, J., Li, Y., Wu, J., Wang, Z., Xie, J., Zhang, Y., Liu, T., Zhang, Y.,

461   Song, B., Ma, W., Liu, Y., Yan, C., Jiang, J., Kerminen, V.-M., Xia, M., Nieminen, T., Du, W., Kokkonen, T., and Kulmala,

462   M.: Measurement report: The 4-year variability and influence of the Winter Olympics and other special events on air quality

463   in urban Beijing during wintertime, Atmos. Chem. Phys., 23, 6663–6690, https://doi.org/DOI10.5194/acp-23-6663-2023,

464   2023.

465   Ho, W. C., Hartley, W. R., Myers, L., Lin, M. H., Lin, Y. S., Lien, C. H., and Lin, R. S.: Air pollution, weather, and associated

466   risk factors related to asthma prevalence and attack rate, Environ. Res., 104, 402–409,

467   https://doi.org/10.1016/j.envres.2007.01.007, 2007.

468   Jeffries, H. E.: An exprimental method for measuring the rate of synthesis, destruction, and transport of ozone in the lower

469   atmosphere, Ph.D. Thesis, Department of Environmental Science and Engineering, University of North Carolina, E.S.E.

470   Publication No.285, 1971.

471   Juda-Rezler, K., Reizer, M., Maciejewska, K., Błaszczak, B., and Klejnowski, K.: Characterization of atmospheric PM$_{2.5}$

472   sources at a Central European urban background site, Sci. Total Environ., 713, 136729,

473   https://doi.org/10.1016/j.scitotenv.2020.136729, 2020.

474   Kanaya, Y.: Photochemical ozone production at a subtropical island of Okinawa, Japan: Implications from simultaneous

475   observations of HO$_2$ radical and NO$_x$, J. Geophys. Res. Atmos., 107, 4368, https://doi.org/10/ckvjkc, 2002.

476   Kleinman, L. I.: A comparative study of ozone production in five U.S. metropolitan areas, J. Geophys. Res., 110, D02301,

477   https://doi.org/10/ft8qfj, 2005.

478   Liu, Y., Xu, X., Yang, X., He, J., Ji, D., and Wang, Y.: Significant reduction in fine particulate matter in Beijing during 2022

479   Beijing Winter Olympics, Environ. Sci. Technol. Lett., 9, 822–828, https://doi.org/10.1021/acs.estlett.2c00532, 2022.

480   Liu, Z., Hu, B., Zhang, J., Yu, Y., and Wang, Y.: Characteristics of aerosol size distributions and chemical compositions during

481   wintertime pollution episodes in Beijing, Atmos. Res., 168, 1–12, https://doi.org/10.1016/j.atmosres.2015.08.013, 2016.

482   Ma, X., Tan, Z., Lu, K., Yang, X., Chen, X., Wang, H., Chen, S., Fang, X., Li, S., Li, X., Liu, J., Liu, Y., Lou, S., Qiu, W.,
483   Wang, H., Zeng, L., and Zhang, Y.: OH and HO_2 radical chemistry at a suburban site during the EXPLORE-YRD campaign
484   in 2018, Atmos. Chem. Phys., 22, 7005–7028, https://doi.org/10.5194/acp-22-7005-2022, 2022.

485   Prinn, R. G.: The cleansing capacity of the atmosphere, Annu. Rev. Environ. Resour., 28, 29–57, https://doi.org/10/b8kg65,
486   2003.

487   Ren, X., Harder, H., Martinez, M., Lesher, R. L., Oliger, A., Simpas, J. B., Brune, W. H., Schwab, J. J., Demerjian, K. L., and
488   He, Y.: OH and HO_2 chemistry in the urban atmosphere of New York City, Atmos. Environ., 3639–3651,
489   https://doi.org/10.1016/s1352-2310(03)00459-x, 2003.

490   Ren, X., van Duin, D., Cazorla, M., Chen, S., Mao, J., Zhang, L., Brune, W. H., Flynn, J. H., Grossberg, N., Lefer, B. L.,
491   Rappenglück, B., Wong, K. W., Tsai, C., Stutz, J., Dibb, J. E., Thomas Jobson, B., Luke, W. T., and Kelley, P.: Atmospheric
492   oxidation chemistry and ozone production: Results from SHARP 2009 in Houston, Texas, J. Geophys. Res. Atmos., 118,
493   5770–5780, https://doi.org/10/f5cwzr, 2013.

494   Ren, Y., Stieger, B., Spindler, G., Grosselin, B., Mellouki, A., Tuch, T., Wiedensohler, A., and Herrmann, H.: Role of the dew
495   water on the ground surface in HONO distribution: a case measurement in Melpitz, Atmos. Chem. Phys., 20, 13069–13089,
496   https://doi.org/10.5194/acp-20-13069-2020, 2020.

497   Sadanaga, Y., Kawasaki, S., Tanaka, Y., Kajii, Y., and Bandow, H.: New system for measuring the photochemical ozone
498   production rate in the atmosphere, Environ. Sci. Technol., 51, 2871–2878, https://doi.org/10/f9qw59, 2017.

499   Schroeder, J. R., Crawford, J. H., Fried, A., Walega, J., Weinheimer, A., Wisthaler, A., Müller, M., Mikoviny, T., Chen, G.,
500   Shook, M., Blake, D. R., and Tonnesen, G. S.: New insights into the column CH_2O/NO_2 ratio as an indicator of near-surface
501   ozone sensitivity, J. Geophys. Res. Atmos., 122, 8885–8907, https://doi.org/10.1002/2017JD026781, 2017.

502   Seinfeld, J. H. and Pandis, S. N.: Atmospheric chemistry and physics: from air pollution to climate change, 2nd ed., John
503   Wiley & Sons, Inc., Hoboken, N.J, 1203 pp., 2006.

504   Sillman, S.: 9.11 - Tropospheric ozone and photochemical smog, in: Treatise on Geochemistry, edited by: Holland, H. D. and
505   Turekian, K. K., Pergamon, Oxford, 407–431, https://doi.org/10.1016/B0-08-043751-6/09053-8, 2003.

506   Sklaveniti, S., Locoge, N., Stevens, P. S., Wood, E., Kundu, S., and Dusanter, S.: Development of an instrument for direct
507   ozone production rate measurements: measurement reliability and current limitations, Atmos. Meas. Tech., 11, 741–761,
508   https://doi.org/10/gmttxc, 2018.

509   Styler, S. A., Brigante, M., D'Anna, B., George, C., and Donaldson, D. J.: Photoenhanced ozone loss on solid pyrene films,
510   Phys. Chem. Chem. Phys., 11, 7876, https://doi.org/10.1039/b904180j, 2009.

511   Tan, Z., Fuchs, H., Lu, K., Hofzumahaus, A., Bohn, B., Broch, S., Dong, H., Gomm, S., Häseler, R., He, L., Holland, F., Li,
512   X., Liu, Y., Lu, S., Rohrer, F., Shao, M., Wang, B., Wang, M., Wu, Y., Zeng, L., Zhang, Y., Wahner, A., and Zhang, Y.:
513   Radical chemistry at a rural site (Wangdu) in the North China Plain: observation and model calculations of OH, HO_2 and
514   RO_2 radicals, Atmos. Chem. Phys., 17, 663–690, https://doi.org/10.5194/acp-17-663-2017, 2017.

515   Tan, Z., Lu, K., Jiang, M., Su, R., Dong, H., Zeng, L., Xie, S., Tan, Q., and Zhang, Y.: Exploring ozone pollution in Chengdu,
516   southwestern China: A case study from radical chemistry to O_3-VOC-NO_x sensitivity, Sci. Total Environ., 636, 775–786,
517   https://doi.org/10.1016/j.scitotenv.2018.04.286, 2018a.

518   Tan, Z., Rohrer, F., Lu, K., Ma, X., Bohn, B., Broch, S., Dong, H., Fuchs, H., Gkatzelis, G. I., Hofzumahaus, A., Holland, F.,
519   Li, X., Liu, Y., Liu, Y., Novelli, A., Shao, M., Wang, H., Wu, Y., Zeng, L., Hu, M., Kiendler-Scharr, A., Wahner, A., and
520   Zhang, Y.: Wintertime photochemistry in Beijing: observations of RO_x radical concentrations in the North China Plain
521   during the BEST-ONE campaign, Atmos. Chem. Phys., 18, 12391–12411, https://doi.org/10.5194/acp-18-12391-2018,
522   2018b.

523   Tan, Z., Lu, K., Jiang, M., Su, R., Wang, H., Lou, S., Fu, Q., Zhai, C., Tan, Q., Yue, D., Chen, D., Wang, Z., Xie, S., Zeng,
524   L., and Zhang, Y.: Daytime atmospheric oxidation capacity in four Chinese megacities during the photochemically polluted
525   season: a case study based on box model simulation, Atmos. Chem. Phys., 19, 3493–3513, https://doi.org/10.5194/acp-19-
526   3493-2019, 2019a.

527   Tan, Z., Lu, K., Hofzumahaus, A., Fuchs, H., Bohn, B., Holland, F., Liu, Y., Rohrer, F., Shao, M., Sun, K., Wu, Y., Zeng, L.,
528   Zhang, Y., Zou, Q., Kiendler-Scharr, A., Wahner, A., and Zhang, Y.: Experimental budgets of OH, HO_2, and RO_2 radicals
529   and implications for ozone formation in the Pearl River Delta in China 2014, Atmos. Chem. Phys., 19, 7129–7150,
530   https://doi.org/10.5194/acp-19-7129-2019, 2019b.

531   Tan, Z., Ma, X., Lu, K., Jiang, M., Zou, Q., Wang, H., Zeng, L., and Zhang, Y.: Direct evidence of local photochemical
532   production driven ozone episode in Beijing: A case study, Sci. Total Environ., 800, 148868, https://doi.org/10/gnzczm,
533   2021.

534   Tang, R., Wu, Z., Li, X., Wang, Y., Shang, D., Xiao, Y., Li, M., Zeng, L., Wu, Z., Hallquist, M., Hu, M., and Guo, S.: Primary
535   and secondary organic aerosols in summer 2016 in Beijing, Atmos. Chem. Phys., 18, 4055–4068,
536   https://doi.org/10.5194/acp-18-4055-2018, 2018.

537   Tarasick, D., Galbally, I. E., Cooper, O. R., Schultz, M. G., Ancellet, G., Leblanc, T., Wallington, T. J., Ziemke, J., Liu, X.,
538   Steinbacher, M., Staehelin, J., Vigouroux, C., Hannigan, J. W., García, O., Foret, G., Zanis, P., Weatherhead, E.,
539   Petropavlovskikh, I., Worden, H., Osman, M., Liu, J., Chang, K.-L., Gaudel, A., Lin, M., Granados-Muñoz, M., Thompson,
540   A. M., Oltmans, S. J., Cuesta, J., Dufour, G., Thouret, V., Hassler, B., Trickl, T., and Neu, J. L.: Tropospheric Ozone
541   Assessment Report: Tropospheric ozone from 1877 to 2016, observed levels, trends and uncertainties, Elemen. Sci. Anthro.,
542   7, 39, https://doi.org/10.1525/elementa.376, 2019.

543   Whalley, L. K., Stone, D., Dunmore, R., Hamilton, J., Hopkins, J. R., Lee, J. D., Lewis, A. C., Williams, P., Kleffmann, J.,
544   Laufs, S., Woodward-Massey, R., and Heard, D. E.: Understanding in situ ozone production in the summertime through
545   radical observations and modelling studies during the Clean air for London project (ClearfLo), Atmos. Chem. Phys., 18,
546   2547–2571, https://doi.org/10.5194/acp-18-2547-2018, 2018.

547   Whalley, L. K., Slater, E. J., Woodward-Massey, R., Ye, C., Lee, J. D., Squires, F., Hopkins, J. R., Dunmore, R. E., Shaw, M.,
548   Hamilton, J. F., Lewis, A. C., Mehra, A., Worrall, S. D., Bacak, A., Bannan, T. J., Coe, H., Percival, C. J., Ouyang, B.,

549   Jones, R. L., Crilley, L. R., Kramer, L. J., Bloss, W. J., Vu, T., Kotthaus, S., Grimmond, S., Sun, Y., Xu, W., Yue, S., Ren,
550   L., Acton, W. J. F., Hewitt, C. N., Wang, X., Fu, P., and Heard, D. E.: Evaluating the sensitivity of radical chemistry and
551   ozone formation to ambient VOCs and NO_x in Beijing, Atmos. Chem. Phys., 21, 2125–2147, https://doi.org/10.5194/acp-
552   21-2125-2021, 2021.

553   Xu, X., Lin, W., Xu, W., Jin, J., Wang, Y., Zhang, G., Zhang, X., Ma, Z., Dong, Y., Ma, Q., Yu, D., Li, Z., Wang, D., and
554   Zhao, H.: Long-term changes of regional ozone in China: implications for human health and ecosystem impacts, Elem. Sci.
555   Anth., 8, 1–27, https://doi.org/10.1525/elementa.409, 2020.

556   Xue, L. K., Wang, T., Guo, H., Blake, D. R., Tang, J., Zhang, X. C., Saunders, S. M., and Wang, W. X.: Sources and
557   photochemistry of volatile organic compounds in the remote atmosphere of western China: results from the Mt. Waliguan
558   Observatory, Atmos. Chem. Phys., 13, 8551–8567, https://doi.org/10/f49wrr, 2013.

559   Xue, M., Ma, J., Tang, G., Tong, S., Hu, B., Zhang, X., Li, X., and Wang, Y.: RO_x budgets and O_3 formation during
560   summertime at Xianghe suburban site in the North China Plain, Adv. Atmos. Sci., 38, 1209–1222, https://doi.org/10/gkf965,
561   2021.

562   Zhou, W., Cohan, D. S., and Henderson, B. H.: Slower ozone production in Houston, Texas following emission reductions:
563   evidence from Texas Air Quality Studies in 2000 and 2006, Atmos. Chem. Phys., 14, 2777–2788,
564   https://doi.org/10.5194/acp-14-2777-2014, 2014.

565   Zhou, X., Gao, H., He, Y., Huang, G., Bertman, S. B., Civerolo, K., and Schwab, J.: Nitric acid photolysis on surfaces in low-
566   NO_x environments: Significant   atmospheric   implications,   Geophys.   Res.   Lett.,   30,   n/a-n/a,
567   https://doi.org/10.1029/2003GL018620, 2003.

568